https://doi.org/10.1016/j.ijheatmasstransfer.2017.11.154

Collision-induced jet-like mixing for droplets of unequal-sizes

Kai Sun[1], Peng Zhang[2,*], Ming Jia[3], and Tianyou Wang[1,*]

[1] *State Key Laboratory of Engines, Tianjin University, Tianjin 300072, China*

[2] *Department of Mechanical Engineering, The Hong Kong Polytechnic University, Hong Kong 999077, China*

[3] *School of Energy and Power Engineering, Dalian University of Technology, Dalian 116024, China*

Abstract

The internal mixing of droplets upon coalescence is of fundamental importance to a number of applications in microfluidics, micro-scale heat and mass transfer, and rocket engine propulsion. Compared to the well-known surface-tension-induced jet-like mixing in the coalescence of inertialess droplets, collision-induced jet-like mixing was observed recently and remains inadequately understood. In the present study, the collision dynamics and internal mixing of droplets of unequal sizes was numerical simulated by using the lattice Boltzmann phase-field method, with emphasis on unraveling the mechanism of the internal jet formation and therefore on exploring strategies to facilitate such a mixing pattern. The results show that the formation of the internal jet requires two synergetic flow motions favoring low *Oh* number and high *We* number: the capillary-pressure-driven radial converging flow induced by the crater restoration to detach the spreading smaller droplet from the surface, and the impact-inertia-driven axial motion along the crater surface to drive the penetration of the detached fluid. The jet-like structure was found to correlate with the evolution of a main vortex ring, which is formed by the vorticity generation on the interface during initial impact, and transported into the droplet during subsequent oscillations. However, due to the absence of the bulge retraction that generates a significant amount of vorticity and to the extended duration for the jet formation, the main vortex is much less intensive compared to that formed by the inertialess droplet coalescence and is therefore less capable of inducing obvious vortex-ring structure in the mixing pattern. Further simulations by manipulating the disparity of the droplet sizes and the disparity of the liquid viscosities show that, the collision of a larger droplet with lower viscosity with a smaller droplet with higher viscosity is effective in facilitating jet-like mixing.

Keywords: Droplet mixing; Vortex dynamics; Lattice Boltzmann method

*To whom correspondence should be addressed: pengzhang.zhang@polyu.edu.hk (Peng Zhang); wangtianyou@tju.edu.cn (Tianyou Wang)

Nomenclature	
C	fluid composition
D	droplet diameter
E_0	bulk free energy
k	gradient factor
L_0	initial distance between the droplets
M	mobility of the interface
p	pressure
t	time
t_0	time of initial coalescence
t_{osc}	characteristic oscillation time of the smaller droplet, $t_{osc}=\sqrt{\rho D_S^3/\sigma}$
t^*	normalized time, $t^* = (t - t_0) / t_{osc}$
$\boldsymbol{u}$	flow velocity
U_0	initial relative velocity between the droplets
$\boldsymbol{U}$	initial velocity of the droplet
β	prefactor of the bulk free energy
ξ	thickness of the liquid-gas interface
ρ	density
μ	dynamics viscosity
μ_C	chemical potential
σ	surface tension coefficient
Subscripts	
L	larger droplet
S	smaller droplet
l	liquid phase
g	gas phase
Nondimensional parameters	
We	*Weber* number, $We = \rho_l U_0^2 D_S / \sigma$
Oh	*Ohnesorge* number, $Oh = \mu_l / \sqrt{\rho_l D_S \sigma}$
Δ	size ratio, $\Delta=D_L/D_S$
ρ^*	density ratio, $\rho^* = \rho_l / \rho_g$
μ^*	viscosity ratio, $\mu^* = \mu_l / \mu_g$

1. Introduction

Droplet collision in a gaseous environment is of fundamental relevance to many natural and industrial processes such as rain/cloud formation, ink-jet printing, spray coating, and spray combustion in engines. For decades, great efforts including experimental [1-6], numerical [7-12], and theoretical investigations [13], have been devoted to unravel the rich phenomena and the multi-scale physics, with emphasis on identifying collision outcomes and their dependence on the collision parameters. It has been well recognized that the colliding droplets, with increasing impact inertia, can lead to the nonmonotonic outcomes of "permanent coalescence with minor deformation" - "bouncing" - "permanent coalescence with large deformation" - "separation subsequent to temporary coalescence", with the coalescence/bouncing transition depending on whether or not the gas film could be sufficiently drained out, and the coalescence/separation transition depending on whether or not the excessive kinetic energy could be held by surface tension.

Recently, there is increasing interest in the internal mixing within the merged droplet, especially for its potential in the applications such as property design in microfluidics [14, 15], rocket engine ignition utilizing gelled hypergolic propellants (GHP) [16], and color manipulation in ink-jet printing [17, 18]. Take the propulsion systems utilizing GHP for instance, since the fuel and the oxidizer are sprayed separately into the combustion chamber, while their vapor pressure are too low to form flammable gaseous mixture due to gelation, ignition could be only triggered by the liquid-phase reactions in the merged droplet containing both fuel and oxidizer liquid mass. Therefore, unraveling and facilitating efficient mixing is critical to the viability of utilizing GHP.

It is noted that the mixing of two identical colliding droplets are restricted by the intrinsic symmetry across the plane of collision, and that droplets with either disparity in the physical properties or in the sizes may result in enhanced mixing by symmetry-breaking. In this regard, Blanchette [19] numerically observed increasingly significant mixing between two equal-sized droplets with surface tension difference as the result of the Marangoni effect. Focke *et al.* [20] investigated both experimentally and numerically on the collision dynamics of droplets with viscosity disparity and observed enhanced mixing. Sun *et al.* [21] numerically simulated the collision of two non-Newtonian droplets and found that the internal mixing is promoted for the droplets with significant rheological difference. Specifically, liquid interpenetration is facilitated

for the droplets with different extent of shear-thinning effect, while permanent coalescence and internal mixing are simultaneously facilitated for the collision between a shear-thinning droplet and a shear-thickening droplet.

Compared with the collision between droplets with distinct physical properties, unequal-sized droplet collision has attracted more attention particularly due to its higher practical relevance, not to mention its intrinsic tendency of promoting permanent coalescence, which is required by the subsequent internal mixing [6]. Anilkumar *et al.* [22] experimentally found that, the inertialess coalescence of a droplet and a liquid pool may lead to a jet-like mixing with an accompanied strong vortex ring. Numerical simulations by Nobari and Tryggvason [23] and Liu *et al.* [24] show that the jet-like mixing is largely affected by the droplet viscosity and can form only at sufficiently small *Ohnesorge* numbers. Sun *et al.* [25] further justified that the formation of the jet-like mixing depends on whether the viscous damping on the capillary wave propagation is small enough to allow a liquid bulge to form before the smaller droplet totally merges into the large one. As a result, lowering the viscosity of the smaller droplet rather than that of the larger droplet is much more effective in facilitating the jet-like mixing. Xia *et al.* [26] analyzed the generation of vorticity inside the merged droplet and found that the emergence of the internal jet is attributed to the formation of a main vortex ring, as the jet-like structure shows a strong correlation with the main vortex ring.

The collision dynamics and internal mixing at larger impact inertia were investigated experimentally by Ashgriz and Poo [27], and numerically by Nikolopoulos *et al.* [28, 29], Sun *et al.* [30], and Chen *et al.* [31]. It is noteworthy that the jet-like mixing was also numerically observed at high *Weber* numbers as long as the *Oh* number is sufficiently small [30, 31] and was experimentally confirmed by Tang *et al.* [32] recently. Their experiments also show the interesting non-monotonic emergency of “jet” - “no jet” - “jet” as the impact inertia increases, suggesting that the two types of jet may be owing to different mechanisms. The experiment by Zhang *et al.* [33] on the hypergolic ignition by head-on collision of N,N,N’,N’-tetramethylethylenediamine and white fuming nitric acid droplets further showed a non-monotonic variation of the ignition delay times with increasing the *We* number. This phenomenon was attributed to the non-monotonic emergence of jet-like mixing, which facilitates the liquid-phase reactions. It is nevertheless noted that, compared to the surface-tension-induced

jet-like mixing identified in low *We* number collisions/coalescences, the collision-induced jet-like mixing at high *We* number collisions still remains inadequately understood.

In the present investigation, we aim to numerically study the high-*We*-number collision of unequal-sized droplets, with particular interest in the formation of internal jet that facilitates mixing. Only head-on collision is taken into consideration, since the jet-like mixing shows no evident correlation with the eccentricity between the droplets [27, 31]. In the following text, the numerical methodology, results and discussion, and concluding remarks are presented sequentially in Secs. 2 to 4.

2. Numerical Methodology

2.1 Problem Specifications

Since the head-on droplet collision is intrinsically symmetric with respect to the axis connecting the centers of mass of the two droplets, an axisymmetric computational domain is employed in the present study. As shown in Fig. 1, two droplets of diameter D_S and D_L (the subscripts S and L denote small and large, respectively) are placed in the initially stationary gaseous environment, with their velocities given by $\boldsymbol{U}_S = -(D_L / D_S)^3 \boldsymbol{U}_L$ so as to zero the total momentum of the binary system. The outflow boundary condition is applied on the domain boundaries except the axis.

2.2 Macroscopic Governing Equations

In the present study, the phase-field multiphase model [34, 35] is employed to capture the liquid-gas interface. The composition C, which stands for the volume fraction of the liquid in the local fluid, is governed by the *Cahn-Hilliard* equation

$$\frac{\partial C}{\partial t} + \boldsymbol{u} \cdot \nabla C = M \nabla^2 \mu_C , \tag{1}$$

where $\boldsymbol{u}$ is the fluid velocity, M the mobility, and $\mu_C = \mu_0 - k\nabla^2 C = \partial E_0 / \partial C - k\nabla^2 C$ the chemical potential with E_0 being the bulk free energy and k the gradient factor. The bulk free energy usually takes a double-well function as $E_0 = \beta C^2 (1-C)^2$, and the chemical potential is therefore given by $\mu_C = \beta(4C^3 - 6C^2 + 2C) - k\nabla^2 C$ [36]. Owing to the diffusion term of Eq. (1), the

interface is always kept close to its equilibrium state, and the surface tension and the interface thickness are determined by $\sigma = \sqrt{2k\beta}/6$ and $\xi = \sqrt{8k/\beta}$, respectively.

The continuity equation and the momentum equation for the incompressible flow are given by

$$\nabla \cdot \boldsymbol{u} = 0, \tag{2}$$

and

$$\rho[\frac{\partial \boldsymbol{u}}{\partial t} + \boldsymbol{u} \cdot \nabla \boldsymbol{u}] = -\nabla p + \nabla \cdot [\mu(\nabla \boldsymbol{u} + \nabla \boldsymbol{u}^{\mathrm{T}})] - C\nabla \mu_C, \tag{3}$$

where p is the pressure and μ the dynamic viscosity. It is noted that the last term on the RHS of Eq. (3) represents the surface tension in its potential form, which is particularly useful to alleviate the discretization error effected by dealing with large density jump across the liquid-gas interface.

2.3. Numerical Implementation

In the present study, the macroscopic governing equations, Eq. (1)-(3), are numerically solved by using the lattice Boltzmann method (LBM) [37, 38]. Two particle distribution functions are employed, with one to capture the liquid-gas interface, and the other to compute the velocity field as well as the dynamic pressure that enforces flow incompressibility [36, 39]. It is worth noting that, the present methodology, by using the potential form of surface tension and the isotropic finite difference, is able to suppress the notorious spurious current to a relatively low level even at large density ratios [26]. Consequently, it has been successfully applied to a variety of droplet dynamics problems, including but not limited to droplet collision [25, 30], droplet impact on surface [36], as well as droplet coalescence [21, 40]. According to our test, the spurious current of the present model is on the order of 10^{-5} (lattice unit, LU), which is significantly smaller than the characteristic velocity of the colliding droplet (on the order of 10^{-2} LU), indicating that the effect of the spurious current is negligible in the present study. The details on deriving the LBM evolution equations for the distribution functions in an axisymmetric coordinate system can be referred to Ref. [30] and will not be repeated here. Furthermore, to visualize the mixing within the coalesced droplet, massless tracer particles are embedded in the smaller droplets for every 1/6 lattice spacing in both axial and radial directions, and the trajectories of the particles are tracked by using the 4th-order Runge-Kutta method.

According to dimensional analysis, the flow similarity of the present problem is exclusively determined by five independent non-dimensional parameters, such as the *Weber* number *We*, the *Ohnesorge* number *Oh*, the size ratio Δ, the density ratio ρ^*, and the viscosity ratio μ^*. In the simulation, ρ^* and μ^* are fixed at the typical values, for water droplets in air, of 833 and 55, respectively, and the collision process is therefore not significantly affected by the ambient gas [5].

Regarding the mesh resolution, the thickness of the liquid-gas interface is fixed at 5 grids, and the diameter of the smaller droplet D_S is consistently resolved by 200 grids to visualize fine structures of the velocity and vorticity fields, although the formation of internal jet shows no evident grid-dependency as long as D_S is resolved by more than 60 grids. In the simulation, time is normalized by $t^* = (t - t_0)/t_{osc}$, where t_0 denotes the onset of coalescence, and $t_{osc} = \sqrt{\rho_l D_S^3/\sigma}$ the characteristic oscillation time of the smaller droplet [26, 32]. It is noted that, the precise determination of t_0 in the simulation could be rather difficult for the approaching diffused interfaces, as such it is approximated by L_0/U_0, where L_0 stands for the initial distance between the droplets. Such simplification does not bring any difference on the physical interpretation of the problem. A typical simulation with the present mesh resolution and for a duration of $t^* = 8$ takes about 400 hours of real time on an Intel 3.5GHz Broadwell CPU.

3. Results and Discussion

3.1 Experimental Verification

The present numerical methodology has been extensively validated against the experiments of droplet collision of both Newtonian [25, 30] and non-Newtonian fluids [25] as well as the internal mixing of inertialess droplet coalescence [21, 30]. For further experimental validation, we simulated the experiment of Tang *et al.* [32] on the internal mixing of unequal-sized droplet collisions. Fig. 2 compares the experimental and simulation results, with Fig. 2 (a) and (b) corresponding to water droplets and Fig. 2(c) to n-tetradecane droplets. As shown in the figures, the present simulation successfully reproduced the emergence of jet-like mixing for water droplets, as the smaller droplet penetrates into the larger droplet in Fig. 2 (a) and (b), and the absence of the jet-like mixing for n-tetradecane droplets, as the smaller droplet remains spreading

on the surface of the larger droplet in Fig. 2 (c).

It should be also noted that, the time sequence of the simulation and the experiment show some differences, which were also observed in the simulation by Tang *et al.* [32]. This is however generally within the experimental error, which is 0.1ms (about 0.3 non-dimensional time) in the early stage of droplet collision and is 0.4-0.5ms (about 1.2-1.5 non-dimensional time) in the late stage of droplet mixing [32]. Overall, the concerned physics of internal jet formation is believed to be correctly captured by the present simulation, substantiating further discussion as follows.

3.2 Formation of Internal Jet

To understand the formation of the internal jet, we employed Fig. 2(a) as the benchmark case and first examined the time evolution of the penetration length, which illustrated in Fig. 3(a), is defined as the maximum distance of the small droplet from the upper interface. As shown in Fig. 3(b), the formation of the jet can be divided into three stages: Stage I (t^*<0.45), a "crater" is formed by the collision, with the smaller droplet spreading on its surface; Stage II (0.45<t^*<2.15), the crater restores by the surface tension, and the smaller droplet converges towards the axis, forming a "dome" that nails into the larger droplet; Stage III, the merged droplet continues oscillating and the jet-like mixing gradually forms with the strengthened interpenetration. It is noted that, the penetration length increases abruptly during Stage II, indicating that the restoration of the crater plays a critical role in the jet formation. This is further substantiated by the collision of n-tetradecane droplets shown in Fig. 2(c), where the smaller droplet remains spreading on the surface of the larger droplet during Stage II and no jet could be formed eventually.

Fig. 4 shows the evolution of the flow field and the pressure distribution during the crater restoration and subsequent oscillation for the benchmark case. It is seen that, at the beginning of the crater restoration, *e.g.* t^*=0.47, the concaved crater effects a significant capillary pressure gradient directing from its rim to its bottom, and thereby induces a strong converging flow towards the axis, as shown in Fig. 5. Consequently, the axially outward motion of the crater mainly carries the liquid from its rim rather than from the axial interior of the droplet, resulting in the convergence of the smaller droplet towards the axis. At t^*=1.12, when the initial crater has transformed into a convex bulge, the axially outward motion is decelerated by the inward capillary pressure gradient, and a recirculation zone appears at the bottom of the smaller droplet

to prevent the penetrated liquid from being pulled back to the surface. During the subsequent droplet oscillation, as illustrated at t^*=2.80 as a representative time, the radially inward retraction of the interface, manifested by the direction of the pressure gradient, drives the internal fluid to spread along the axis, and the penetration length is consequently increased. It is noted that, the bottom of the smaller droplet is not significantly shifted in the sub-figures, and the increase of the penetration length is therefore mainly ascribed to the retracting motion of the interface. This is fundamentally different from the inertialess coalescence, in which the internal jet is formed by the advancing motion of the smaller droplet driven by the capillary pressure difference [21, 32].

Recognizing the critical role of the surface-tension-driven flow, especially the radially converging flow during Stage II in facilitating the jet formation, we can explain why such jet-like mixing was not observed for n-tetradecane droplet collision shown in Fig. 2(c): because of the high *Oh* number, the capillary force is largely counteracted by the viscous force, and hence no significant radial converging flow could be generated.

It is already shown that the impact inertia plays a critical role in forming the crater during Stage I. Subsequently, the jet formation is caused by the surface-tension-governed oscillation during Stages II and III. To answer the question that whether or not the inertia is indispensable during the two later stages, we deliberately devised a contrastive simulation by resetting the entire flow field of the benchmark case to zero at the beginning of Stage II, as shown in Fig. 6(b), and found that no jet-like mixing was formed. Compared with the benchmark case in Fig. 6(a), the restoration of the crater and subsequent oscillation in the contrastive case is much more intensive, and the smaller droplet only follows the interfacial oscillation without deeply penetrating into the larger droplet, indicating that significant role of the impact inertia during the later stages.

Fig. 7 shows the axial velocity distribution within the droplet at the beginning of Stage II of the benchmark case (t^*=0.47). It is seen that, while the center of the crater has started to restore by surface tension to produce a small upward velocity, a considerable amount of impact inertia still remains on its rim and thereby generates an axial relative motion in the vicinity of the crater surface. As discussed above, the restoration of the crater is mainly supplied by the liquid from the rim rather than from the axially interior of the larger droplet, the remaining inertia along the rim would largely slow down the crater restoration, as illustrated by the comparison of Fig. 6(a) and

Fig. 6(b), and provide additional axial stretching motion on the both ends of the penetrated smaller droplet, which should be responsible for the aforementioned observation of a recirculation zone at t^*=1.12 in Fig. 4. Therefore, in addition to the surface-tension-driven radially converging flow that transports the spreading smaller droplet towards the axis, the axial flow motion along the crater caused by impact inertia is also essential in propelling the penetration to facilitate internal jet formation. This finally explains why such jet-like mixing was observed in the droplet collision with simultaneously a low *Oh* number and a considerable *We* number.

3.3 Vortex Dynamics during Jet Formation

The above discussion has clarified how the internal jet forms, while it does not answer the question why such a jet-like mixing is accompanied with a vortex ring that is significantly weaker than that as observed in the inertialess droplet coalescence, in which the jet-like structure was found to correlate strongly with a main vortex ring inside the merged droplet [26]. According to Helmholtz's third theorem [41], vorticity cannot be generated within the droplet of homogeneous fluid without a rigid boundary, but it can be generated on the free liquid-gas interface. Therefore, further attention should be paid to how vorticity is generated on the interface and transported into the interior of the droplet.

Fig. 8 shows the vorticity distribution within the merged droplet of the benchmark case, where the three stages in the sub-figures are consistent with the previous classification, and the vorticity is normalized by $\omega^* = \omega t_{osc}$ [26]. As shown in the figure, the formation of the internal jet is indeed related to the vorticity field, as the leading front of the penetrated smaller droplet is accompanied with a main vortex of positive intensity, which can been clearly identified at t^*=3.0. Specifically, in the very early time of Stage I, *e.g.* t^*=0.03, the liquid bridge connecting the two droplets expands rapidly, and a pair of strongly counter-rotating vortices are generated in the vicinity of the interface, with the anticlockwise one on the smaller droplet side corresponding to the main vortex. However, as the liquid bridge develops, its concave-shape shortly transforms into a convex-shape as shown at t^*=0.15. Such a transformation of the interface geometry is critical to the fate of the main vortex, as an opposite pair of counter-rotating vortices are generated along the newly-formed convex surface and the head of the main vortex is therefore

detached from the interface. During the subsequent time of Stage I, the head of the main vortex is passively transported by the droplet spreading while weakened due to unavoidable viscous dissipation, and the main vortex can be still strengthened by the positive vorticity generation from its tail to prevent it from accumulating into a concentrated vortex ring.

During Stage II, the radially converging flow generates negative vorticity along the surface of the crater, and the main vortex is therefore detached integrally from the interface and then transported into the interior of the droplet. It is noted that, at t^*=2.0 when the smaller droplet has sufficiently penetrated into the larger droplet, the intensity of the main vortex has significantly weakened compared with that during Stage I.

During Stage III, take one cycle of droplet oscillation for instance, although another vortex with positive vorticity is generated by the radial retraction along the crater at t^*=4.1 and is detached from the interface at t^*=4.5, its subsequent transport to the droplet interior is dominated by the flow induced by droplet elongation and it cannot deeply penetrate into the droplet to merge with main vortex. Therefore, the main vortex will be dissipated without being enhanced by the interfacial oscillation, and its leading front therefore grows thicker instead of developing into an evident vortex-ring structure.

Finally, to supplement the above disucssion, the jet-like mixing of the nearly inertialess droplet coalesecne was simulated with the same *Oh* number and size ratio of the benchmark case for comparison. Here the *We* number was set to a small value of 0.1 to trigger coalesence. As shown in Fig. 9, the formation of the vortex-ring structure observed at t^*=1.5 is accompanied with a main vortex substantially stronger than that of the benchmark case. Regarding the source of the main vortex, in contrary to the benchmark case with large *We* number where the main vortex is formed by the vorticity generation during the liquid bridge expansion, the main vortex in inertialess droplet coalesence is mainly formed by the significant vorticity generation during the bugle retraction as illustrated at t^*=0.75 in Fig. 9. Secondly, regarding the duration, the formation of internal jet in droplet collision is an intrinsic consequence of the interfacial deformation and internal flow motion caused by impact, whose time scale should be estimated by $t_{impact} \sim D_S/U_0$. In contrast, the internal jet formed in inertialess droplet coalescence is driven solely by surface tension and its timescale should be estimated by $t_{coalescence} \sim t_{osc} = \sqrt{\rho D_S^3 / \sigma}$. By comparing these

two timescales, we have $t_{impact} / t_{coalescence} \sim (D_S / U_0) / \sqrt{\rho D_S^3 / \sigma} = \sqrt{\sigma / (\rho U_0^2 D_S)} = \sqrt{1/We}$, which explains why the formation of internal jet in inertialess droplet coalescence is much faster than that in droplet collision with *We*~O(10). As such, for the collision-induced jet-like mixing, since the main vortex can be only fed by vorticity generation during Stage I, its retarded transport into the interior of the droplet and the associated excessive dissipation, during the prolonged jet formation, makes it much less intensive to entrain fluid to form vortex-ring structure in the mixing pattern.

3.4 Enhancement of Jet-like Mixing

Having understood the mechanism of internal jet formation in the unequal-sized droplet collision, we further explore how to enhance such jet-like mixing. Particular interest is given to manipulate the disparity of liquid viscosities to match with the disparity of droplet sizes, which could be readily realized in many applications, for example the GHP rocket engines where the fuel and the oxidizer are gelled and injected separately. It is noted that lowering the viscosity of the smaller droplet rather than that of the larger droplet was found to be much more effective in enhancing the jet-like mixing formed in inertialess droplet coalescence [21]. Since the mechanism of internal jet formation is different in the present problem, the applicability of the same strategy is questionable and merits investigation.

Fig. 10 shows the collision dynamics and internal mixing of droplets at fixed *We*=20 and Δ=2.0 while with different viscosities. To account for the differences in the droplet viscosity, we use $Oh_S = \mu_S / \sqrt{\rho_l D_S \sigma}$ and $Oh_L = \mu_L / \sqrt{\rho_l D_S \sigma}$ to denote the *Oh* number of the smaller droplet and the larger droplet, respectively. As shown in Fig. 10(a) with Oh_S=Oh_L=0.1, the high viscous dissipation greatly suppresses the droplet deformation and no significant mixing is resulted. If Oh_S is decreased to 0.01, as illustrated in Fig. 10(b), the smaller droplet would spread much more widely on the surface of the crater, but it could not further converge into the interior of the larger droplet to form a jet during the subsequent droplet oscillation. As a result, the successful strategy of mixing enhancement for inertialess droplet coalescence is inapplicable to the present problem.

Remembering that the formation of the internal jet requires both the radially converging flow to detach the smaller droplet from the crater surface and the considerable axial flow to drive

the penetration of the smaller droplet, we may hypothesize that lowering the viscosity of the larger droplet will strengthen these flows and thereby facilitate the jet-like mixing. As shown in Fig. 11, compared to the case (a) with Oh_S=Oh_L=0.1, the decrease in the viscosity of the larger droplet indeed facilitates the internal jet formation, as dome-like mixing is observed with Oh_L=0.02 and jet-like mixing emerges with Oh_L=0.002. In Fig. 11(c), the internal jet could be rapidly formed during Stage II, as the larger droplet of small viscosity is able to retain considerable kinetic energy and thereby to strongly wedge the smaller droplet of large viscosity from the outer edge.

The above investigation suggests that the strategy of facilitating jet-like mixing for droplet collision should be fundamentally different from that for inertialess droplet coalescence, and the lower-viscosity liquid should be sprayed into droplet with larger sizes instead of the opposite way as reported in Ref. [21].

4. Concluding Remarks

In the present study, the jet-like mixing in the high-*We*-number collision of unequal-sized droplets was numerically investigated by using the lattice Boltzmann method. The phase-field multiphase model was employed to capture the liquid-gas interface, and massless particles were tracked by using the 4th-order Runge-Kutta method to visualize the internal mixing of the droplet. The simulation successfully reproduced the previous experimental observations of internal jet formation in the collision of water droplets and n-tetradecane droplets.

The simulation shows that the internal jet is formed during the restoration of the collision-generated crater and the subsequent droplet oscillation. Two critical flow motions are identified, namely the capillary-pressure-driven radially converging flow during the crater restoration, which detaches the spreading smaller droplet from the surface towards the axis, and the axial relative motion along the crater surface resulted by the remaining impact inertia, which generates additional stretching effect on the both ends of the penetrated smaller droplet. The generation and development of both flows require low *Oh* number and high *We* number, at which the jet-like mixing was only observed.

The vortex dynamics analysis shows that the jet-like structure is correlated with the evolution of a main vortex ring, which is formed by the vorticity generation on the interface

during initial impact, and transported into the droplet interior during subsequent droplet oscillations. However, compared with the previously studied inertialess droplet coalescence, in which the bulge retraction generates a significant amount of vorticity and a shorter duration for jet formation, the weaker main vortex in high-*We*-number droplet collisions are less capable of inducing evident vortex-ring structure.

With the understanding of the mechanism for internal jet formation, parametric studies were conducted by manipulating the disparity of liquid viscosities to match with the disparity of droplet sizes and to explore the possible strategy for mixing enhancement. The results show that, in contrast with the inertialess droplet coalescence, the collision of a larger droplet with lower viscosity with a smaller droplet with higher viscosity tends to facilitate the jet-like mixing.

Acknowledgements

This work was financially supported by the National Natural Science Foundation of China (No. 51606134) and the National Natural Science Funds for Distinguished Young Scholar (No. 51525603). The work at the Hong Kong Polytechnic University was sponsored by Hong Kong RGC/GRF (PolyU 152217/14E and PolyU 152651/16E).

References

[1] P.R. Brazier-Smith, S.G. Jennings, J. Latham, The interaction of falling water drops: coalescence, Proc. R. Soc. Lond. A 326 (1972) 393-408.

[2] G. Brenn, A. Frohn, Collision and coalescence of droplets of various liquids, J. Aerosol. Sci. 20 (1989) 1027-1030.

[3] J. Qian, C.K. Law, Regimes of coalescence and separation in droplet collision, J. Fluid Mech. 331 (1997) 59-80.

[4] K.D. Willis, M.E. Orme, Experiments on the dynamics of droplet collisions in a vacuum, Exp. Fluids 29 (2000) 347-358.

[5] K.L. Pan, C.K. Law, B. Zhou, Experimental and mechanistic description of merging and bouncing in head-on binary droplet collision, J. Appl. Phys. 103 (2008) 064901.

[6] C.L. Tang, P. Zhang, C.K. Law, Bouncing, coalescence, and separation in head-on collision of unequal-size droplets, Phys. Fluids 24 (2012) 022101.

[7] K.N. Premnath, J. Abraham, Simulations of binary drop collisions with a multiple-relaxation-time lattice-Boltzmann model, Phys. Fluids 17 (2005) 122105.

[8] N. Nikolopoulos, K.S. Nikas, G. Bergeles, A numerical investigation of central binary collision of droplets, Comput. Fluids 38 (2009) 1191-1202.

[9] K. Sun, M. Jia, T.Y. Wang, Numerical investigation of head-on droplet collision with lattice Boltzmann method, Int. J. Heat Mass Transf. 58 (2013) 260-275.

[10] D. Lycett-Brown, K.H. Luo, R.H. Liu, P.M. Lv, Binary droplet collision simulations by a multiphase cascaded lattice Boltzmann method, Phys. Fluids 26 (2014) 023303.

[11] C.K. Kuan, K.L. Pan, W. Shyy, Study on high-Weber-number droplet collision by a parallel, adaptive interface-tracking method, J. Fluid Mech. 759 (2014) 104-133.

[12] G. Finotello, J.T. Padding, N.G. Deen, A. Jongsma, F. Innings, J.A.M. Kuipers, Effect of viscosity on droplet-droplet collisional interaction, Phys. Fluids 29 (2017) 067102.

[13] P. Zhang, C.K. Law, An analysis of head-on droplet collision with large deformation in gaseous medium, Phys. Fluids 23 (2011) 042102.

[14] A.M. Nightingale, T.W. Phillips, J.H. Bannock, J.C. de Mello, Controlled multistep synthesis in a three-phase droplet reactor, Nat. Commun. 5 (2014) 3777.

[15] A.B. Theberge, E. Mayot, A.E. Harrak, F. Kleinschmidt, W.T.S. Huck, A.D. Griffiths, Microfluidic platform for combinatorial synthesis in picolitre droplets, Lab Chip 12 (2012) 1320-1326.

[16] C.K. Law, Fuel options for next-generation chemical propulsion, AIAA J. 50 (2012) 19-36.

[17] H. Minemawari, T. Yamada, H. Matsui, J. Tsutsumi, S. Haas, R. Chiba, R. Kumai, T. Hasegawa, Inkjet printing of single-crystal films, Nature 475 (2011) 364-367.

[18] S. Fathi, P. Dickens, Challenges in drop-on-drop deposition of reactive molten nylon materials for additive manufacturing, J. Mater. Process. Technol. 213 (2013) 84-93.

[19] F. Blanchette, Simulation of mixing within drops due to surface tension variations, Phys. Rev. Lett. 105 (2010) 074501.

[20] C. Focke, M. Kuschel, M. Sommerfeld, D. Bothe, Collision between high and low viscosity droplets: Direct numerical simulations and experiments, Int. J. Multiphase Flow 56 (2013) 81-92.

[21] K. Sun, T.Y. Wang, P. Zhang, C.K. Law, Non-Newtonian flow effects on the coalescence and mixing of initially stationary droplets of shear-thinning fluids, Phys. Rev. E 91 (2015) 023009.

[22] A.V. Anilkumar, C.P. Lee, T.G. Tang, Surface-tension-induced mixing following coalescence of initially stationary drops, Phys. Fluids A 3 (1991) 2587.

[23] M.R. Nobari, G. Tryggvason, The flow induced by the coalescence of two initially stationary drops, NASA Technical Report No. 19950007240 (1994).

[24] D. Liu, P. Zhang, C.K. Law, Y.C. Guo, Collision dynamics and mixing of unequal-size droplets, Int. J. Heat Mass Transf. 57 (2013) 421-428.

[25] K. Sun, P. Zhang, C.K. Law, T.Y. Wang, Collision Dynamics and Internal Mixing of Droplets of Non-Newtonian Liquids, Phys. Rev. Appl. 4 (2015) 054013.

[26] X. Xia, C. He, D. Yu, J. Zhao, P. Zhang, Vortex-ring-induced internal mixing upon the coalescence of initially stationary droplets, Phys. Rev. Fluids, in press.

[27] N. Ashgriz, J.Y. Poo, Coalescence and separation in binary collisions of liquid drops, J. Fluid Mech. 221 (1990) 183-204.

[28] N. Nikolopoulos, G. Bergeles, The effect of gas and liquid properties and droplet size ratio on the central collision between two unequal-size droplets in the reflexive regime, Int. J. Heat Mass Transf. 54 (2011) 678-691.

[29] N. Nikolopoulos, G. Strotos, K.S. Nikas, G. Bergeles, The effect of Weber number on the central binary collision outcome between unequal-sized droplets, Int. J. Heat Mass Transf. 55 (2012) 2137-2150.

[30] K. Sun, M. Jia, T.Y. Wang, Numerical investigation on the head-on collision between unequal-sized droplets with multiple-relaxation-time lattice Boltzmann model, Int. J. Heat Mass Transf. 70 (2014) 629-640.

[31] X.D. Chen, D.J. Ma, V. Yang, Collision outcome and mass transfer of unequal-sized droplet collision, in Proceedings of 50th AIAA Aerospace Sciences Meeting including the New Horizons Forum and Aerospace Exposition, Nashville, 2012.

[32] C.L. Tang, P. Zhang, C.K. Law, Z.H. Huang, Dynamics of internal jet in the mixing of droplets of unequal sizes, J. Fluid Mech. 795 (2016) 671-689.

[33] D. Zhang, P. Zhang, Y. Yuan, T. Zhang, Hypergolic ignition by head-on collision of N,N,N',N'-tetramethylethylenediamine and white fuming nitric acid droplets, Combust. Flame 173 (2016) 276-287.

[34] D. Jacqmin, Calculation of two-phase Navier-Stokes flows using phase-field modeling, J. Comput. Phys. 155 (1999) 96-127.

[35] P. Yue, J.J. Feng, C. Liu, J. Shen, A diffuse-interface method for simulating two-phase flows of complex fluids, J. Fluid Mech. 515 (2004) 293-317.

[36] T. Lee, L. Liu, Lattice Boltzmann simulations of micronscale drop impact on dry surfaces, J. Comput. Phys. 229 (2010) 8045-8063.

[37] R. Benzi, S. Succi, M. Vergassola, The lattice Boltzmann equation: theory and applications, Phys. Rep. 222 (1992) 145-197.

[38] S. Chen, G.D. Doolen, Lattice boltzmann method for fluid flows, Annu. Rev. Fluid Mech. 30 (1998) 329-364.

[39] T. Lee, Effects of incompressibility on the elimination of parasitic currents in the lattice Boltzmann equation method for binary fluids, Comput. Math. Appl. 58 (2009) 987-994.

[40] L. Baroudi, S.R. Nagel, J.F. Morris, T. Lee, Dynamics of viscous coalescing droplets in a saturated vapor phase, Phys. Fluids 27 (2015) 121702.

[41] P.G. Saffman, Vortex dynamics, Cambridge university press, Cambridge, 1992.

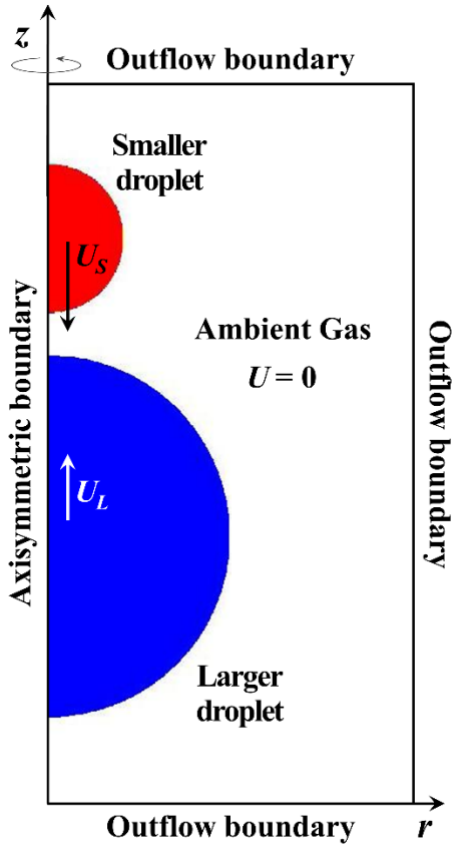

Fig. 1. Specifications of computational domain and boundary conditions.

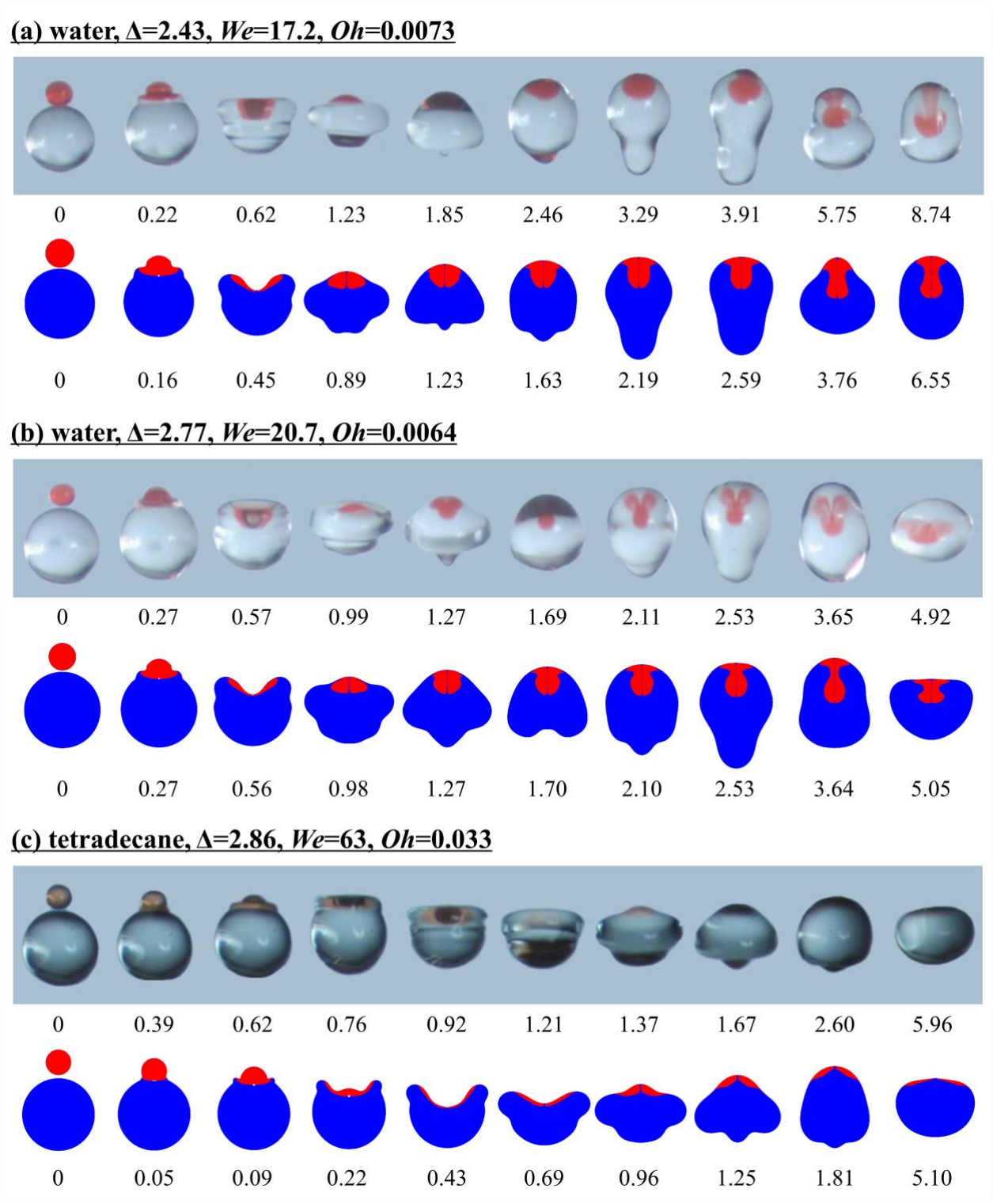

Fig. 2. Experimental verification of the collision dynamics and internal mixing of unequal-sized droplets. (a) water, Δ=2.43, *We*=17.2, *Oh*=0.0073, (b) water, Δ=2.77, *We*=20.7, *Oh*=0.0064, (c) tetradecane, Δ=2.86, *We*=63, *Oh*=0.033. The experimental images are adapted from Ref. [32].

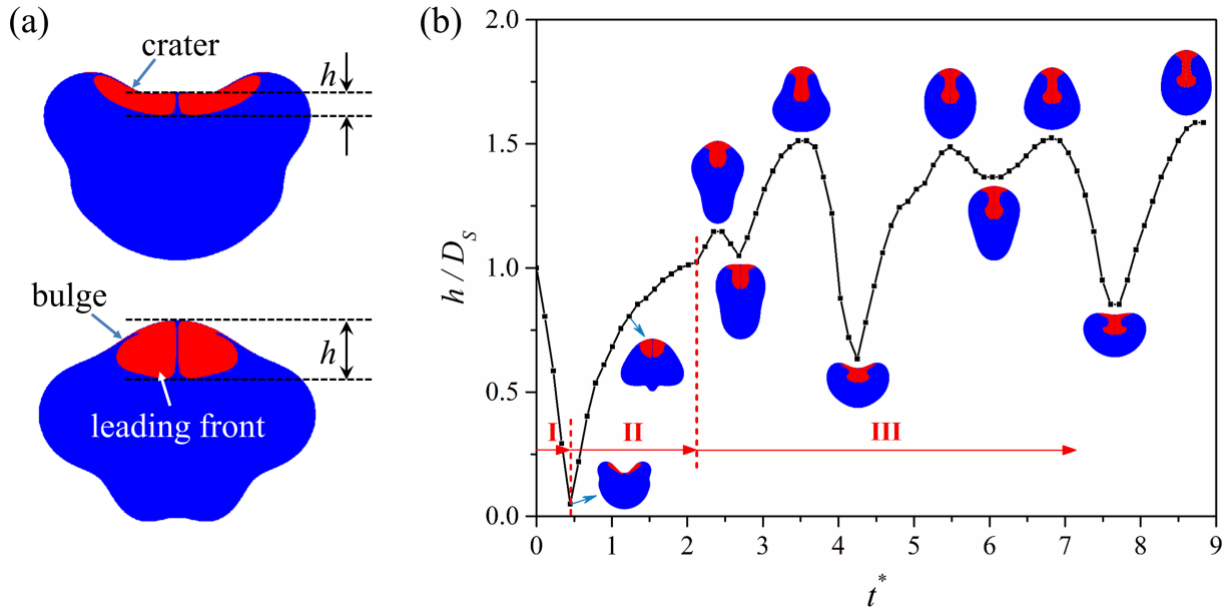

Fig. 3. Evolution of the penetration length of the smaller droplet into the larger droplet. (a) definition of the penetration length *h*, (b) time evolution of the penetration length for case (a) in Fig. 2.

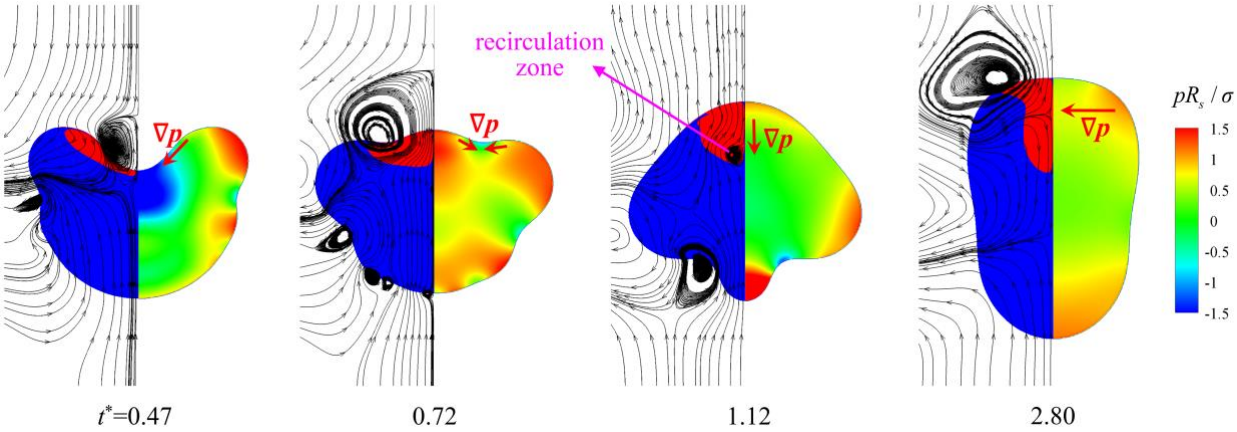

Fig. 4. Evolution of the flow field and the pressure distribution during Stage II for the benchmark case. In the sub-figures, the left halves denote the flow field and the mixing pattern, and the right halves the pressure distribution.

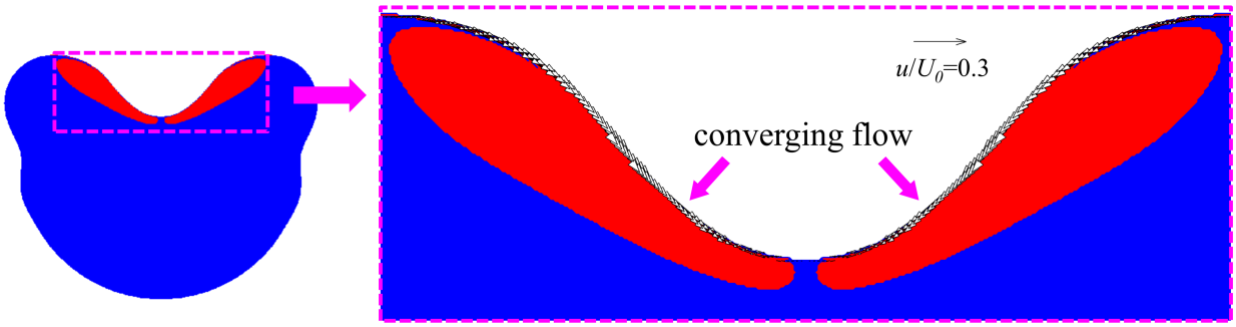

Fig. 5. The tangential velocity on the interface of the concaved crater at t^*=0.47 of the benchmark case.

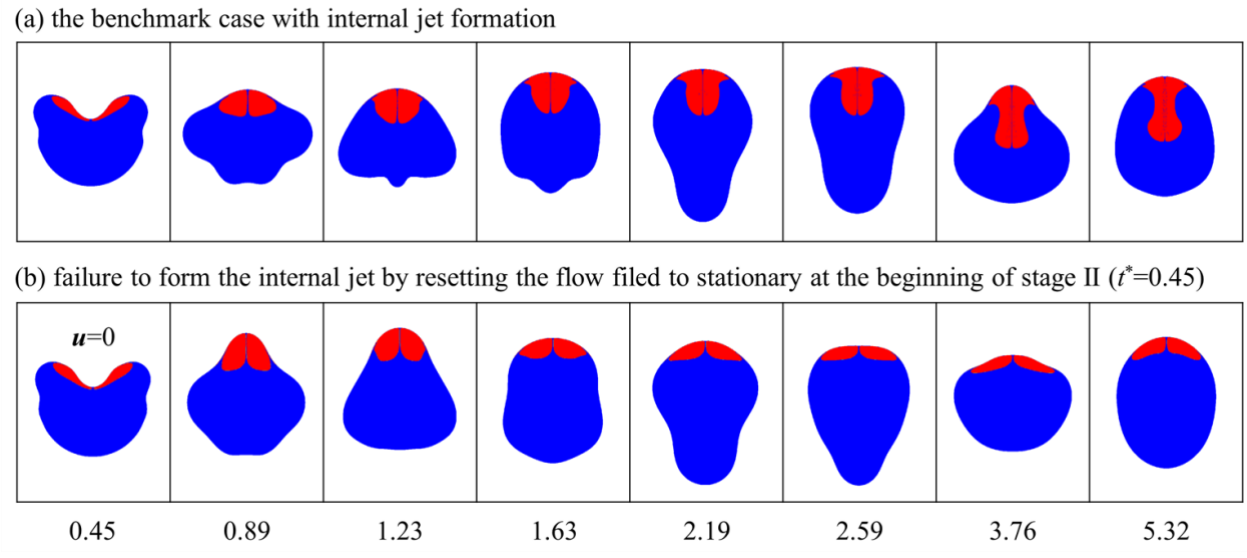

Fig. 6. Comparison of (a) the benchmark case and (b) a contrastive case by resetting the entire flow field to zero at the beginning of Stage II.

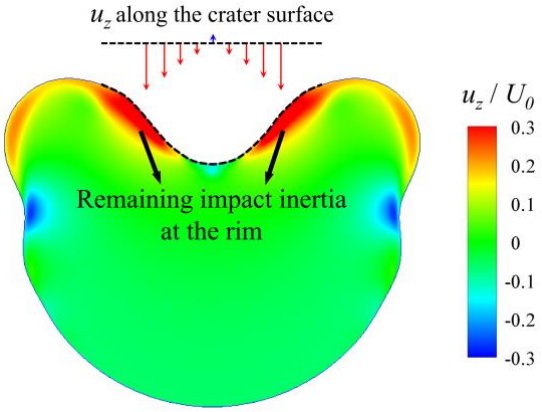

Fig. 7. The axial velocity distribution within the droplet at the beginning of the crater restoration (t^*=0.47) of the benchmark case.

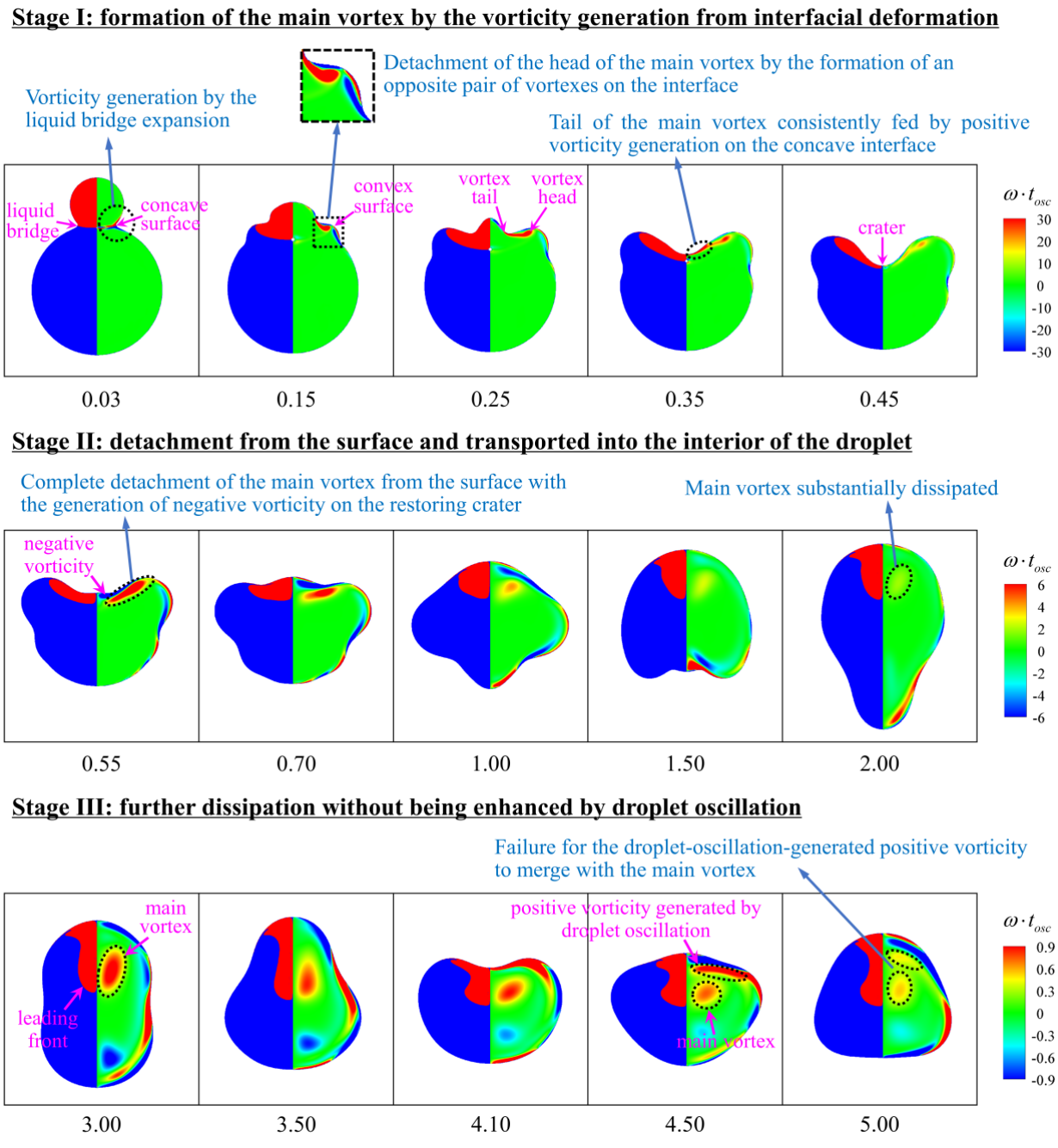

Fig. 8. The vortex dynamics for the benchmark case at *We*=17.2, *Oh*=0.0073, and Δ=2.43. In the sub-figures, the left halves denote the mixing, and the right halves the vorticity distribution.

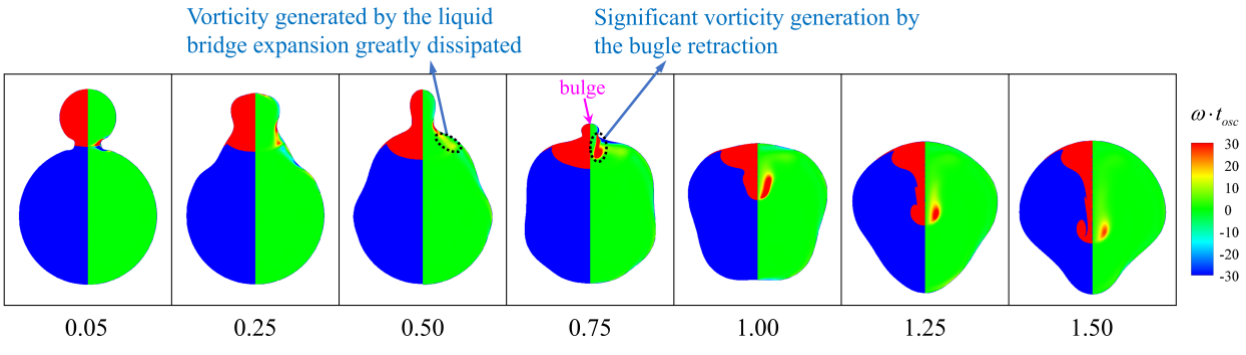

Fig. 9. The vortex dynamics of droplet coalescence at *We*=0.1, *Oh*=0.0073, and Δ=2.43. In the sub-figures, the left halves denote the mixing, and the right halves the vorticity distribution.

(a) Oh_L=Oh_S=0.1, two droplets are equally high viscous

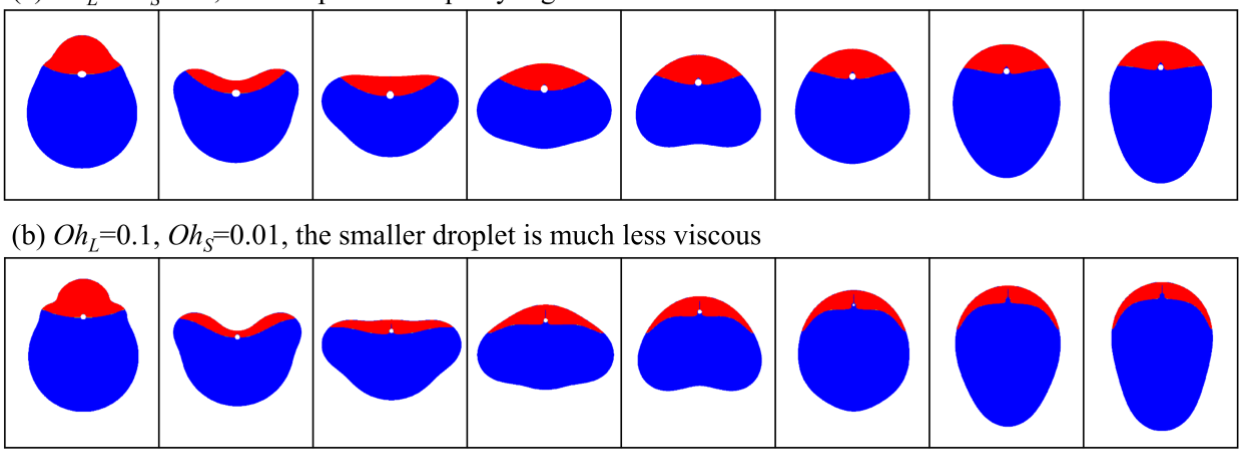

(b) Oh_L=0.1, Oh_S=0.01, the smaller droplet is much less viscous

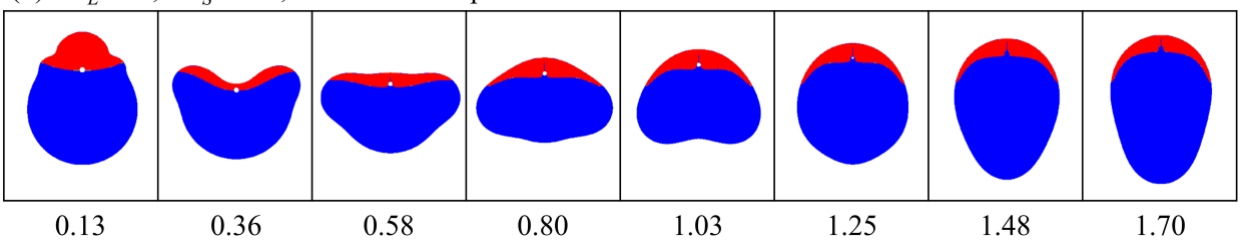

0.13 0.36 0.58 0.80 1.03 1.25 1.48 1.70

Fig. 10. Collison dynamics and internal mixing of droplets at different *Oh* numbers (a) Oh_L=Oh_S=0.1, (b) Oh_L=0.1, Oh_S=0.01, and fixed *We*=20 and Δ=2.0.

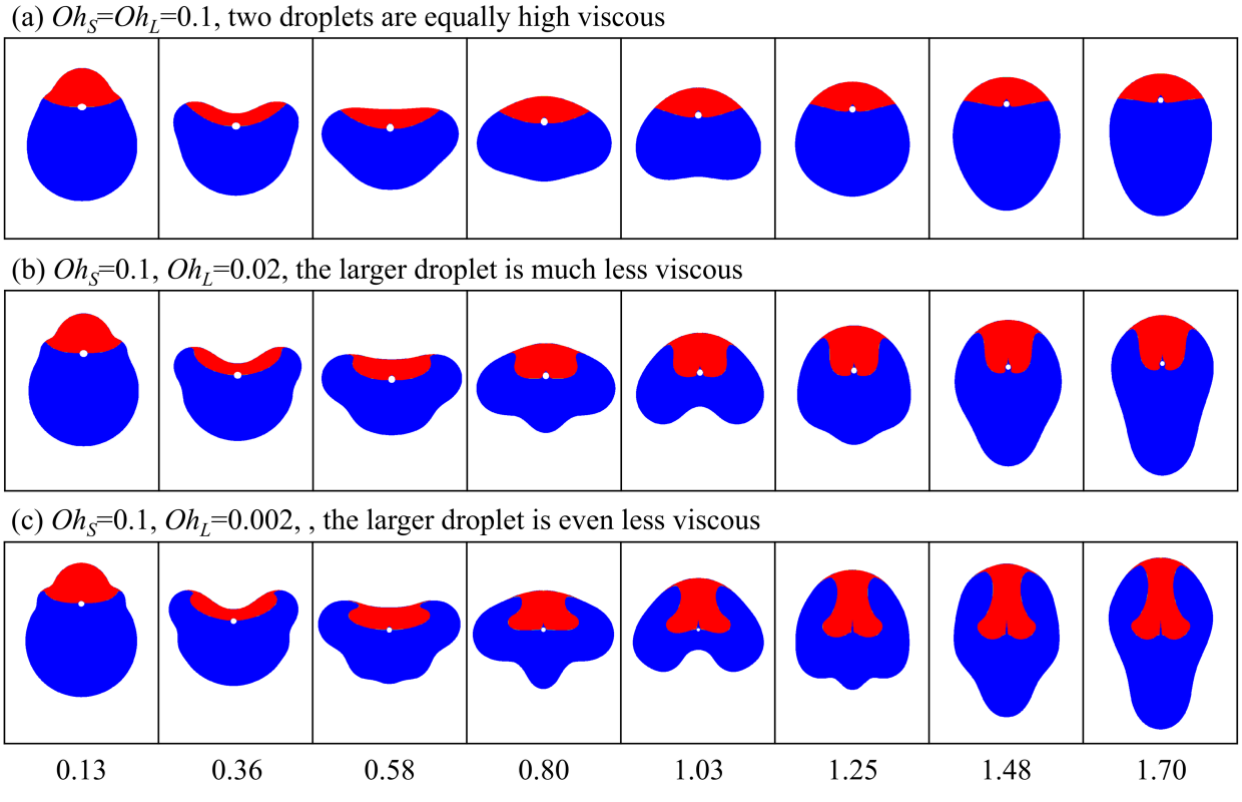

Fig. 11. Collison dynamics and internal mixing of droplets at different *Oh* numbers (a) Oh_S=Oh_L=0.1, (b) Oh_S=0.1, Oh_L=0.02, (c) Oh_S=0.1, Oh_L=0.002, and fixed *We*=20 and Δ=2.0.